RSC Advances

PAPER

View Article Online
View Journal | View Issue

Cite this: *RSC Adv.*, 2024, **14**, 30582

Mechanism and toxicity assessment of carbofuran degradation by persulfate-based advanced oxidation process†

Chenxi Zhang, [ab] Youxin Xu,[ab] Bingbing Chu[a] and Xiaomin Sun *[b]

The advanced oxidation process based on persulfate has been proven to be a promising method for degrading the highly toxic carbamate pesticide carbofuran (CBF). However, the mechanism of CBF degradation by sulfate radicals ($SO_4\cdot^-$) and hydroxyl radicals (·OH) is still unclear and requires further research and discussion. This study investigated the mechanism and toxicity assessment of CBF degradation using density functional theory (DFT) theory calculation methods. The results indicated that $SO_4\cdot^-$ and ·OH can undergo addition and abstraction reactions with CBF. Thermodynamic and kinetic analysis showed that the abstraction reaction between $SO_4\cdot^-$ and the secondary H atom is the optimal reaction pathway, exhibiting the highest branching ratio (Γ = 41.84%). The rate constants for the reactions of CBF with $SO_4\cdot^-$ and ·OH at room temperature were found to be 3.66×10^9 and 8.96×10^8 M^{-1} s^{-1}, respectively, which are consistent with experimental data reported in previous studies. The acute and chronic toxicity of CBF and its degradation products to aquatic organisms was predicted through an ecological toxicity assessment model. The toxicity of the degradation products was lower than that of the parent CBF, confirming the viability of using persulfate-based advanced oxidation processes for water treatment.

Received 24th July 2024
Accepted 19th September 2024

DOI: 10.1039/d4ra05365f

rsc.li/rsc-advances

1 Introduction

Carbofuran (CBF) is a broad-spectrum systemic *N*-methyl carbamate pesticide widely used as an insecticide, nematicide, and acaricide in agriculture, household, and industrial sectors.[1,2] It belongs to the highly toxic pesticides among all *n*-methyl carbamate insecticides, posing significant acute toxicity to humans.[3,4] CBF is particularly hazardous to birds among various environmental organisms.[5,6] When raptors, small mammals, or reptiles feed on small birds that have been poisoned to death by carbofuran, it can cause secondary poisoning and lead to death. CBF is soluble in water and highly mobile in soil, with a long half-life of up to 50 ∼ 110 days.[7,8] And it can contaminate groundwater and nearby water bodies through precipitation runoff.[9] Research indicates that exposure to CBF concentrations of 0.0044 mg L^{-1} or higher for more than 7 days in aquatic environments can alter the histology of gills, liver, and kidneys in Nile tilapia, thereby compromising fish health.[10] Moreover, studies suggest serious neurological damage in humans associated with CBF, potentially linking it to cancer.[11] Therefore, due to its endocrine-disrupting effects and neurotoxic inhibition, CBF poses high risks to aquatic ecosystems and public health, emphasizing the critical need to control its presence in aquatic environments.

Currently, methods for removing CBF from drinking water and wastewater mainly include adsorption, bioremediation, and chemical degradation.[12–16] Sugarcane bagasse-peanut shell magnetic composites, bamboo shoot shell-based activated carbon, and coated polystyrene beads have been studied for their adsorption capabilities in water containing CBF.[17–19] While these methods show promising results, effective treatment of the waste and pollutants generated during the adsorption process is currently lacking, posing environmental risks.[20] Additionally, bioremediation is considered a time-consuming process.[21,22] Therefore, chemical degradation is seen as a viable approach for treating CBF-contaminated water bodies, particularly through persulfate-based advanced oxidation processes (AOPs).[23] Many laboratory and field studies have shown that persulfate-based AOPs has been widely applied to pesticide pollutants in the environment, such as dimethoate, ethyl-parathion, atrazine, and imidacloprid.[24–27] This technology generates reactive oxygen species (ROS) such as sulfate radicals ($SO_4\cdot^-$, E^0 = 2.5–3.1 V), which have a higher redox potential compared to hydroxyl radicals (·OH, E^0 = 2.8 V).[28] Additionally, $SO_4\cdot^-$ has a longer half-life, faster kinetics, greater stability, and a larger transport distance, can operate over

[a]*Shandong Provincial University Laboratory for Protected Horticulture, Weifang University of Science and Technology, Weifang 262700, China*
[b]*Environment Research Institute, Shandong University, Qingdao 266200, P. R. China. E-mail: sxmwch@sdu.edu.cn*

† Electronic supplementary information (ESI) available. See DOI: https://doi.org/10.1039/d4ra05365f

a broader pH range.[29] Therefore, it represents a promising technology for the treatment of organic pollutants.

In general, the ROS produced during the activation process of persulfates vary depending on the activation method used. These species primarily include $SO_4\cdot^-$, ·OH, singlet oxygen ($^1O_2$), and superoxide anions ($O_2\cdot^-$).[30] Accurately analyzing the ROS in AOPs is crucial for understanding the degradation mechanisms of pollutants. Identification methods include electron paramagnetic resonance (EPR), high performance liquid chromatography (HPLC), fluorescence probes, and quenching experiments.[31] EPR is effective in detecting reactive species in water but cannot detect surface-bound radicals.[32] HPLC is affected by various factors in complex systems, and its accuracy needs further improvement.[31] Fluorescence probe methods can be interfered with by background light sources when detecting $^1O_2$.[33] Quenching experiments, as a simple and effective ROS detection method, not only identify the types of ROS but also calculate and analyze their contribution rates and concentrations, and have been widely used in ROS detection.[34] Samy *et al.* synthesized a novel nanocomposite of magnetite for the first time, combining photocatalysis with persulfate activation to synergistically generate more radicals, achieving a degradation efficiency of 92.8% for CBF in a short time.[23] Through quenching experiments, with the addition of the ethanol ($SO_4\cdot^-$ scavenger), isopropanol (·OH scavenger), sodium azide ($^1O_2$ scavenger) and benzoquinone ($O_2\cdot^-$ scavenger), the degradation efficiency decreased to 28.8%, 46%, 90.3% and 80.4%, respectively, confirming the crucial roles of ·OH and $SO_4\cdot^-$. Jiang *et al.* developed cobalt-based catalysts to activate persulfate for CBF degradation, determining the contributions of ·OH and $SO_4\cdot^-$ through quenching experiments and EPR tests.[35] Persulfate technology rapidly oxidizes and decomposes recalcitrant CBF, achieving effective treatment with better environmental and safety profiles compared to other chemical degradation methods. However, the precise mechanism of persulfate technology for CBF degradation remains unclear and requires further research and discussion.

Density functional theory (DFT) calculations can assist in studying the mechanism of radical reactions and in researching the kinetic processes of reactions.[36,37] Atifi *et al.* studied the photodegradation of CBF in aqueous medium using DFT method and explained the dissociation behavior after irradiation based on thermodynamic analysis of the bond dissociation energy of CBF.[38] According to the calculations, the photodegradation of CBF is predicted to occur through the C–O bond cleavage in the carbamate moiety. The results of the Laser Flash Photolysis (LFP) experiment showed the generation of phenoxyl groups, which is consistent with the theoretical calculations. Ćwieląg-Piasecka *et al.* applied DFT method to study the oxidation reaction of CBF with ·OH, where hydrogen atom transfer is the preferred mechanism.[39] Currently, there is no theoretical study on CBF with $SO_4\cdot^-$, and research on the interaction with ·OH is limited to initiation steps, with the degradation mechanism remaining unclear. Therefore, this study proposes to use DFT calculations to investigate the degradation mechanisms of CBF with $SO_4\cdot^-$ and ·OH. In addition, in many cases, products formed during degradation often exhibit higher toxicity than the parent compounds.[40,41] Thus, ecological toxicity assessments also explore the potential environmental risks of CBF and its products. These findings will provide theoretical support for the treatment of CBF wastewater using persulfate oxidation.

2 Computational methods

All geometrical optimizations involved in the degradation process were performed using Gaussian 16 program.[42] The geometric configurations of reactants (R), intermediates (IM), transition states (TS), and products (P) were optimized at the M06-2X/6-31+G(d,p) level of theory. Previous studies have shown that M06-2X is one of the best functionals for a combination of main-group thermochemistry and kinetics.[43,44] For more accurate energy evaluations, single-point energy calculations were performed at the M06-2X/6-311++G(3df,3pd) level on all structures. To account for solvent effects in the entire system, the solvation model density (SMD) model based on self-consistent reaction field theory was employed.[45]

KisThelP software, based on transition state theory (TST) and Wigner tunneling correction, was used for the kinetic calculations.[46,47] The thermodynamic equivalent of eqn (1) is employed in KiSThelP.[46]

$$k^{\mathrm{TST}}(T) = \sigma \frac{k_b T}{h} e^{-\frac{\Delta G^{0,\neq}(T)}{k_b T}} \quad (1)$$

Where σ is the reaction path degeneracy, k_b is the Boltzmann's constant, T is the temperature, h is the Planck's constant, $\Delta G^{0,\neq}(T)$ represents the standard Gibbs free energy of activation for the considered reaction.

Lastly, toxicity assessments of CBF and its degradation products were conducted using the Ecological Structure Activity Relationship (ECOSAR) predictive model.[48] In the model, fish, water fleas, and green algae were selected as aquatic organisms to assess acute and chronic toxicity risks. Acute toxicity to fish and water fleas was evaluated using the median lethal concentration (LC50), indicating the concentration at which 50% of fish and water fleas die after 96 hours and 48 hours of exposure, respectively. The acute toxicity to green algae was determined using the median effective concentration (EC50), representing the concentration at which 50% of the algae show adverse effects after 96 hours of exposure.

3 Results and discussion

3.1 Structural analysis of CBF

The structure of CBF is depicted in Fig. 1(a), with each atom numbered for clarity. In the structure of CBF, there is a phenyl ring, a furan ring, an amino formate group, and three methyl groups. To elucidate the sensitivity of its potential reaction sites, we plotted the electrostatic potential (ESP) distribution of CBF in Fig. 1(b) and highlighted the Fukui function (f^0) and dual descriptor (CDD) values of CBF in Table 1.

In the ESP distribution map, red and blue colors represent electron-deficient and electron-rich regions of CBF, respectively. It can be observed that the phenyl ring and the carbamate group

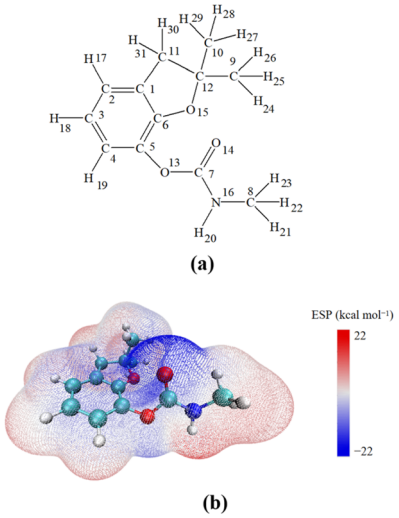

Fig. 1 (a) The structure of CBF. (b) Molecular surface ESP distribution diagram of CBF.

Table 1 Condensed f^0 and CDD indices for CBF

Atom	f^0	CDD	Atom	f^0	CDD
1(C)	0.0341	−0.0513	17(H)	0.0269	−0.0199
2(C)	0.0312	−0.0267	18(H)	0.0324	−0.0370
3(C)	0.0674	−0.1068	19(H)	0.0354	−0.0046
4(C)	0.0281	−0.0385	20(H)	0.1086	0.1935
5(C)	0.0319	−0.0626	21(H)	0.0983	0.1685
6(C)	0.0400	−0.0760	22(H)	0.0283	0.0466
7(C)	0.0279	0.0498	23(H)	0.0615	0.0946
8(C)	0.0494	0.0797	24(H)	0.0050	−0.0037
9(C)	0.0109	−0.0121	25(H)	0.0149	−0.0085
10(C)	0.0097	−0.0049	26(H)	0.0216	−0.0130
11(C)	0.0122	−0.0116	27(H)	0.0183	−0.0101
12(C)	0.0054	−0.0087	28(H)	0.0179	0.0001
13(O)	0.0189	−0.0138	29(H)	0.0111	−0.0033
14(O)	0.0198	0.0249	30(H)	0.0222	−0.0159
15(O)	0.0622	−0.1301	31(H)	0.0215	−0.0212
16(N)	0.0232	0.0150			

have lower electrostatic potential values, making them susceptible to attack by electrophilic reactive oxygen species $SO_4\cdot^-$ and ·OH. According to the values of f^0 and CDD for CBF, higher f^0 values indicate greater susceptibility to attack by reactive radicals, while more negative CDD values suggest greater susceptibility of that region to attack by electrophilic reagents.[49] The f^0 values at C_3 and C_6 positions on the phenyl ring are highest, and the CDD values at C_3 and C_6 on the phenyl ring are most negative, indicating that these are the sites most susceptible to attack by $SO_4\cdot^-$ and ·OH. Furthermore, the f^0 value at O_{15} position is relatively high, and its CDD value is the lowest, suggesting it is susceptible to attack by reactive radicals or electrophilic reagents. However, being a saturated site, it makes it difficult for it to react with radicals.

In addition, $SO_4\cdot^-$ and ·OH are highly oxidative and readily undergo hydrogen atom abstraction reactions.[36] Therefore, the next focus will primarily be on the addition reactions of $SO_4\cdot^-$ and ·OH with the phenyl ring and the C=O bond in the formate group, as well as their hydrogen atom abstraction reactions.

3.2 The addition reaction of CBF with $SO_4\cdot^-$ and ·OH

Fig. 2 and 3 illustrate the addition reactions of CBF with $SO_4\cdot^-$ and ·OH, respectively. In the figures, $\Delta G^{\neq}$ represents the Gibbs free energy barrier, and $\Delta_r G$ denotes the change in Gibbs free energy of the reaction, measured in kcal mol^{-1}. The transition state configurations of CBF reacting with $SO_4\cdot^-$ and ·OH are depicted in Fig. S1 and S2,† respectively.

For the addition reaction of CBF with $SO_4\cdot^-$, the analysis of $\Delta G^{\neq}$ and $\Delta_r G$ for all C positions on the phenyl ring was conducted. It is observed that $\Delta G^{\neq}$ ranges between 2.11 and 6.49 kcal mol^{-1}. Notably, the $\Delta G^{\neq}$ values at the C_3 and C_6 positions are the lowest, at 2.11 and 2.76 kcal mol^{-1}, respectively. This is consistent with the results obtained from the analysis using f^0 and CDD values.

Apart from the $\Delta_r G$ value being positive at the C_1 position, all others are negative, indicating that the addition reaction of $SO_4\cdot^-$ with the phenyl ring is spontaneous. The addition reaction of $SO_4\cdot^-$ with the C=O bond in the formate group shows a $\Delta G^{\neq}$ of 22.35 kcal mol^{-1}, indicating that the potential barrier is much higher than that of the addition reaction with the phenyl ring. The $\Delta_r G$ is 17.42 kcal mol^{-1}, which is positive, indicating that the reaction cannot proceed spontaneously.

The addition reaction of CBF with ·OH, as shown in Fig. 3, follows a pathway similar to the addition reaction with $SO_4\cdot^-$. The $\Delta G^{\neq}$ for the addition to the phenyl ring ranges from 5.39 to 8.98 kcal mol^{-1}, with the lowest $\Delta G^{\neq}$ still observed at the C_3 and C_6 positions. All reactions exhibit negative $\Delta_r G$ values, indicating that the addition of ·OH to the phenyl ring of CBF is spontaneous. Through the analysis of $\Delta G^{\neq}$ and $\Delta_r G$, it is evident that the addition reaction of ·OH with the C=O bond in the formate group presents a higher energy barrier ($\Delta G^{\neq}$ =

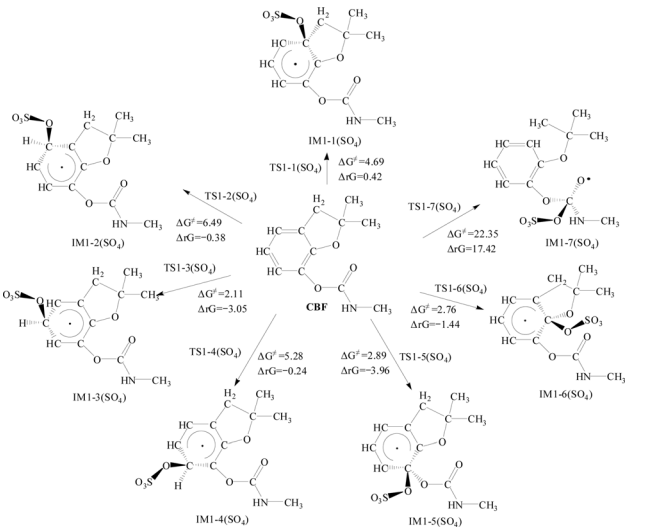

Fig. 2 The Gibbs free energy barrier $\Delta G^{\neq}$ (kcal mol^{-1}) and the Gibbs free energy change $\Delta_r G$ (kcal mol^{-1}) at 298 K for the addition pathways of CBF with $SO_4\cdot^-$.

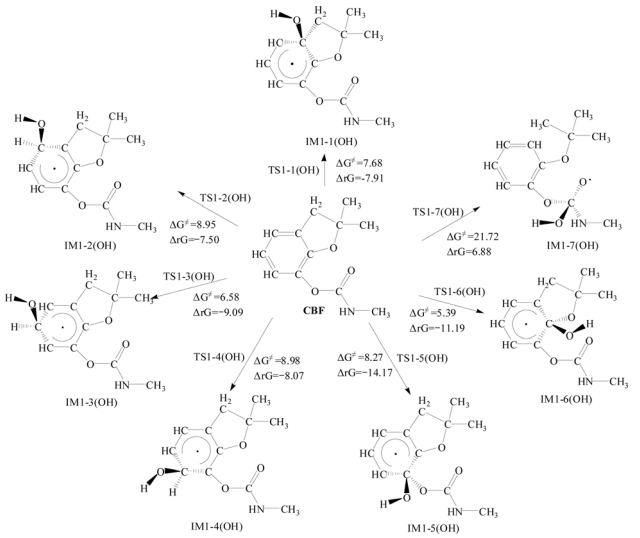

Fig. 3 The Gibbs free energy barrier $\Delta G^{\neq}$ (kcal mol^{-1}) and the Gibbs free energy change $\Delta_r G$ (kcal mol^{-1}) at 298 K for the addition pathways of CBF with ·OH.

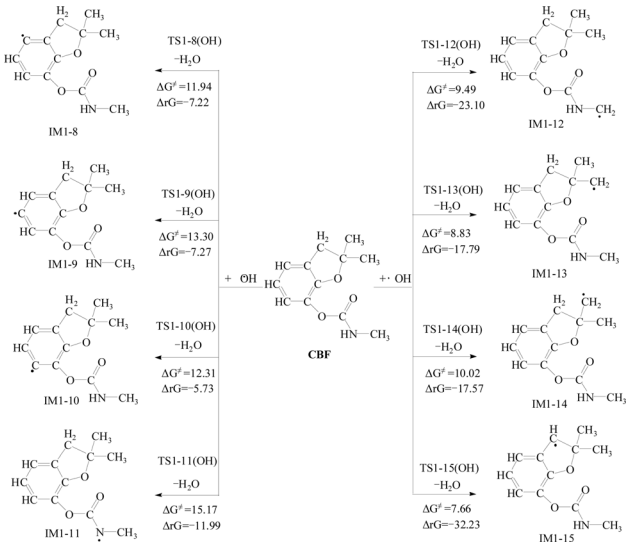

Fig. 5 The Gibbs free energy barrier $\Delta G^{\neq}$ (kcal mol^{-1}) and the Gibbs free energy change $\Delta_r G$ (kcal mol^{-1}) at 298 K for the abstraction reactions of CBF with ·OH.

21.72 kcal mol^{-1}) and is non-spontaneous ($\Delta_r G$ = 6.88 kcal mol^{-1}).

3.3 The abstraction reaction of CBF with $SO_4\cdot^-$ and ·OH

Due to the strong oxidizing properties of $SO_4\cdot^-$ and ·OH, they are prone to undergo hydrogen (H) atom abstraction reactions. There are four types of H atoms on CBF: H atoms on the phenyl ring (H_{17}, H_{18}, and H_{19}), H atom on the amino group (H_{20}), primary H atoms ($H_{21} \sim H_{29}$), and secondary H atoms (H_{30} and H_{31}). The specific reaction pathways are shown in Fig. 4 and 5.

For the H atom abstraction reactions between CBF and $SO_4\cdot^-$, the $\Delta G^{\neq}$ for H atom abstract from the phenyl ring is between 19.05 to 21.99 kcal mol^{-1}, with $\Delta_r G$ being negative or close to negative; for H atom abstract from the amino group, the $\Delta G^{\neq}$ is 11.20 kcal mol^{-1}, with $\Delta_r G$ of −4.75 kcal mol; for the abstraction reactions of primary H atoms, the $\Delta G^{\neq}$ ranges from 11.37 to 14.24 kcal mol^{-1}, while the $\Delta_r G$ ranges from −10.40 to −15.86 kcal mol; for the abstraction reactions of secondary H atoms, $\Delta G^{\neq}$ is 1.54 kcal mol^{-1}, with $\Delta_r G$ of −24.99 kcal mol^{-1}. From a thermodynamic perspective, the activation barrier for secondary H atoms abstraction has the lowest potential barrier and is most likely to occur spontaneously.

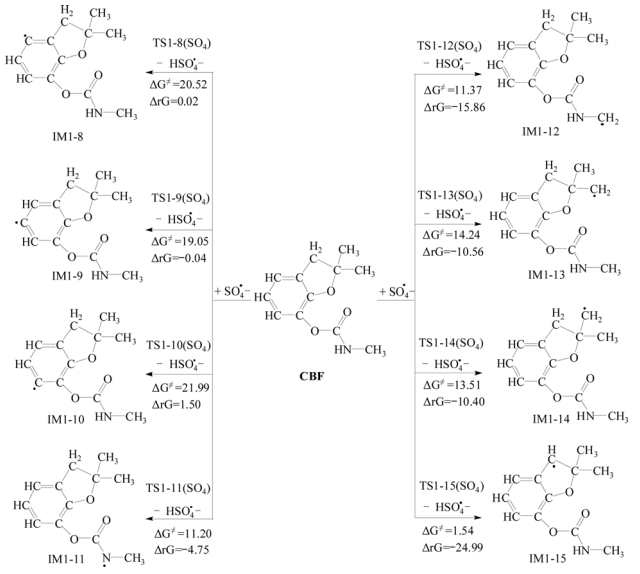

Fig. 4 The Gibbs free energy barrier $\Delta G^{\neq}$ (kcal mol^{-1}) and the Gibbs free energy change $\Delta_r G$ (kcal mol^{-1}) at 298 K for the abstraction reactions of CBF with $SO_4\cdot^-$.

Similar results are observed for the H atom abstraction reactions between CBF and ·OH, with the order of $\Delta G^{\neq}$ being the abstraction reactions of secondary H atoms < the abstraction reactions of primary H atoms < H atom abstract from the phenyl ring < H atom abstract from the amino group. This research result is consistent with the findings on ·OH and the carbamate insecticide isoprocarb, where H atoms are more easily abstracted from the –$CH(CH_3)_2$ and –CH_3 groups than from the –CONH– group and the aromatic ring.[50] Additionally, Xu *et al.* studied the reactions of *N*,*N*-diethyl-*m*-toluamide with $SO_4\cdot^-$ and ·OH at the M06-2X/6-31 + G(d,p) level, found that hydrogen abstraction from –CH_2– is easier than from –CH_3–, which is consistent with our findings.[20] For the abstraction reactions of secondary H atoms, $\Delta G^{\neq}$ is 7.66 kcal mol^{-1}, which is higher than the reaction with $SO_4\cdot^-$. Therefore, from a thermodynamic perspective, the abstraction reaction of CBF with $SO_4\cdot^-$ is slightly easier compared to that of ·OH.

3.4 Rate constants analysis

At 298 K, the rate constants (k) for the reactions of CBF with $SO_4\cdot^-$ and ·OH were calculated, including all possible addition and abstraction reactions. The calculation results are shown in Table 2. In the table, k_{add} represents the rate constant for addition reactions of $SO_4\cdot^-$ and ·OH, k_{abs} represents the rate

Table 2 The k and Γ for in the reaction of CBF with ·OH and $SO_4\cdot^-$ at 298 K

Reaction	k_{298K} (M^{-1} s^{-1})	Γ (%)	Reaction	k_{298K} (M^{-1} s^{-1})	Γ (%)
CBF + $SO_4\cdot^-$ → IM1-1(SO_4)	2.46×10^7	0.54	CBF + ·OH → IM1-1(OH)	1.49×10^7	0.33
CBF + $SO_4\cdot^-$ → IM1-2(SO_4)	2.88×10^6	0.06	CBF + ·OH → IM1-2(OH)	1.89×10^6	0.04
CBF + $SO_4\cdot^-$ → IM1-3(SO_4)	1.09×10^9	23.86	CBF + ·OH → IM1-3(OH)	1.03×10^8	2.26
CBF + $SO_4\cdot^-$ → IM1-4(SO_4)	1.99×10^7	0.44	CBF + ·OH → IM1-4(OH)	1.81×10^6	0.04
CBF + $SO_4\cdot^-$ → IM1-5(SO_4)	1.47×10^8	3.22	CBF + ·OH → IM1-5(OH)	5.54×10^6	0.12
CBF + $SO_4\cdot^-$ → IM1-6(SO_4)	4.73×10^8	10.38	CBF + ·OH → IM1-6(OH)	7.93×10^8	16.20
CBF + $SO_4\cdot^-$ → IM1-7(SO_4)	2.77×10^{-4}	0	CBF + ·OH → IM1-7(OH)	9.13×10^{-4}	0
$k_{add}SO_4\cdot^-$	1.75×10^9	38.51	k_{add}·OH	8.66×10^8	18.99
CBF + $SO_4\cdot^-$ → IM1-8 + $HSO_4\cdot^-$	1.42	0	CBF + ·OH → IM1-8 + H_2O	3.95×10^4	0
CBF + $SO_4\cdot^-$ → IM1-9 + $HSO_4\cdot^-$	1.07×10^1	0	CBF + ·OH → IM1-9 + H_2O	5.36×10^3	0
CBF + $SO_4\cdot^-$ → IM1-10 + $HSO_4\cdot^-$	1.89×10^{-2}	0	CBF + ·OH → IM1-10 + H_2O	9.48×10^3	0
CBF + $SO_4\cdot^-$ → IM1-11 + $HSO_4\cdot^-$	8.49×10^3	0	CBF + ·OH → IM1-11 + H_2O	1.87×10^2	0
CBF + $SO_4\cdot^-$ → IM1-12 + $HSO_4\cdot^-$	4.46×10^4	0	CBF + ·OH → IM1-12 + H_2O	1.65×10^6	0.04
CBF + $SO_4\cdot^-$ → IM1-13 + $HSO_4\cdot^-$	3.61×10^2	0	CBF + ·OH → IM1-13 + H_2O	4.31×10^6	0.10
CBF + $SO_4\cdot^-$ → IM1-14 + $HSO_4\cdot^-$	1.24×10^3	0	CBF + ·OH → IM1-14 + H_2O	5.82×10^5	0.01
CBF + $SO_4\cdot^-$ → IM1-15 + $HSO_4\cdot^-$	1.91×10^9	41.84	CBF + ·OH → IM1-15 + H_2O	2.32×10^7	0.51
$k_{abs}SO_4\cdot^-$	1.91×10^9	41.84	k_{abs}·OH	2.98×10^7	0.66

constant for abstraction reactions of $SO_4\cdot^-$ and ·OH, and Γ represents the branching ratio. The calculation formula for Γ is $\Gamma = k_i/k_{total}$, where k_{total} is the sum of the rate constants for addition and abstraction reactions of $SO_4\cdot^-$ and ·OH with CBF.

Analysis of the calculation results reveals that the abstraction reaction between $SO_4\cdot^-$ and secondary H atom has the highest Γ (41.84%). Next are the addition reactions of $SO_4\cdot^-$ at the C_3 position of the benzene ring (Γ = 23.86%), the addition reactions of ·OH at the C_6 position of the benzene ring (Γ = 16.20%), the addition reactions of $SO_4\cdot^-$ at the C_6 position of the benzene ring (Γ = 10.38%), the addition reactions of $SO_4\cdot^-$ at the C_5 position of the benzene ring (Γ = 3.22%), the addition reactions of ·OH at the C_3 position of the benzene ring (Γ = 2.26%), and the abstraction reaction between ·OH and secondary H atom (Γ = 0.51%). The other reaction pathways can be considered negligible. At 298 K, the calculated total rate constants for the reaction of CBF with $SO_4\cdot^-$ and ·OH are 3.66×10^9 and 8.96×10^8 M^{-1} s^{-1}, respectively. Zhang *et al.* experimentally measured the rate constant of CBF and ·OH to be 9.4×10^7 M^{-1} s^{-1}, which is an order of magnitude lower than the theoretical value.[51] This may be due to the fact that theoretical calculations are typically based on simplified reaction mechanism models, while actual reactions may involve more complex intermediate steps or parallel reactions. Due to the lack of experimental data for CBF with $SO_4\cdot^-$, we compared it with the experimental rate constant of phenylurea with $SO_4\cdot^-$, approximately 5×10^9 M^{-1} s^{-1}, which is consistent with our calculated value.[52,53] These results indicate that the calculated results and subsequent theoretical analysis are reliable and valuable.

In summary, based on the analysis of thermodynamic and kinetic results, it is evident that the abstraction reaction between $SO_4\cdot^-$ and secondary H atom is the optimal reaction pathway. Additionally, the addition reactions of $SO_4\cdot^-$ at the C_3 and C_6 positions of the benzene ring, as well as the addition reactions of $SO_4\cdot^-$ at the C_5 position, cannot be ignored. Therefore, we will focus on studying the subsequent reactions of IM1-3(SO_4), IM1-6(SO_4), IM1-3(OH), IM1-6(OH), IM1-5(SO_4), and IM1-15.

3.5 Subsequent reactions of main intermediates

The reaction pathways of the addition products IM1-3(OH) and IM1-3(SO_4) are similar, both of which can be abstracted by $SO_4\cdot^-$ and ·OH to form stable structures. The specific path is shown in Fig. 6.

IM1-3(OH) and IM1-3(SO_4) can proceed with very low barriers to form products P1 and P2. P1 was detected during the activation of persulfate degradation experiments using nano-magnetite/ZnO/activated carbon nanohybrid.[23] However, the sulfate-originated product P2 was not detected in the experiment, which may be due to its weak stability and rapid evolution into hydroxylated compounds through substitution.[54] The $\Delta_r G$ of this process is negative, indicating that the reaction will proceed spontaneously.

IM1-6(OH) and IM1-6(SO_4) undergo bond cleavage reactions by breaking the C_6–O_{15} bond, thereby opening the furan ring. As shown in Fig. 7, the $\Delta G^{\neq}$ of these two reaction processes is relatively high, measured at 23.96 and 24.01 kcal mol^{-1}

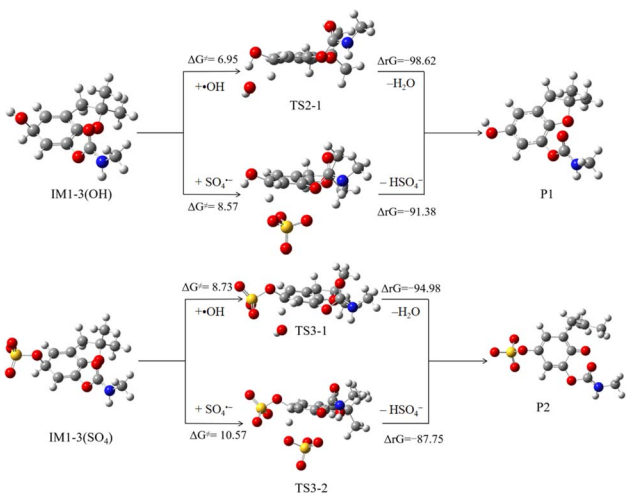

Fig. 6 Subsequent reactions of IM1-3(OH) and IM1-3(SO_4).

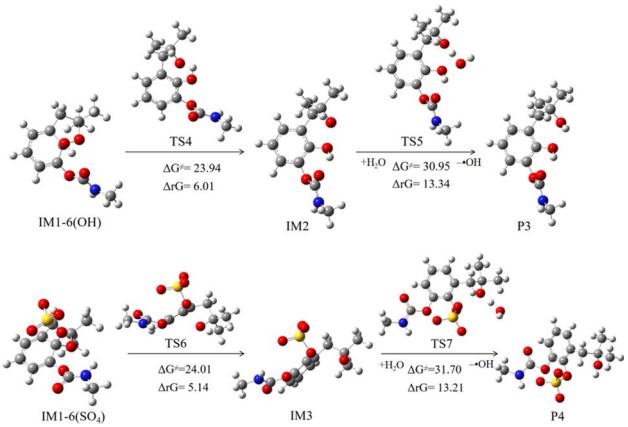

Fig. 7 Subsequent reactions of IM1-6(OH) and IM1-6(SO_4).

respectively. The $\Delta_r G$ is positive, indicating that the reaction will not proceed spontaneously. P3 and P4 were not detected in the experiment, which also confirms that the reaction is difficult to proceed.[23]

The subsequent reaction of IM1-5(SO_4) is depicted in Fig. 8. This process involves initially overcoming a barrier of 10.35 kcal mol^{-1} and releases a significant amount of heat, making it easily spontaneous. This process yields products P5 and intermediate IM4, which can abstract an H atom from the water in the system to obtain stable product P6. The sulfate-originated product P5 has weak stability, will rapidly convert into hydroxylated compounds.[23] The P6 is carbamic acid, which has been proven to decompose into carbon dioxide and methylamine.[55]

The abstraction product IM1-15, with the highest branching ratio, can rapidly undergo barrier-free addition reactions with ·OH present in the system to form stable product P7, releasing a substantial amount of heat. Subsequently, as depicted in Fig. 7, P7 can continue to undergo addition reactions with ·OH. The addition at the C_5 position facilitates the formation of small molecule products through bond cleavage. The $\Delta G^{\neq}$ for this addition process is low, at 10.61 kcal mol^{-1}, and the $\Delta_r G$ is negative, indicating that the reaction will readily proceed spontaneously. After bond cleavage, product P8 will be

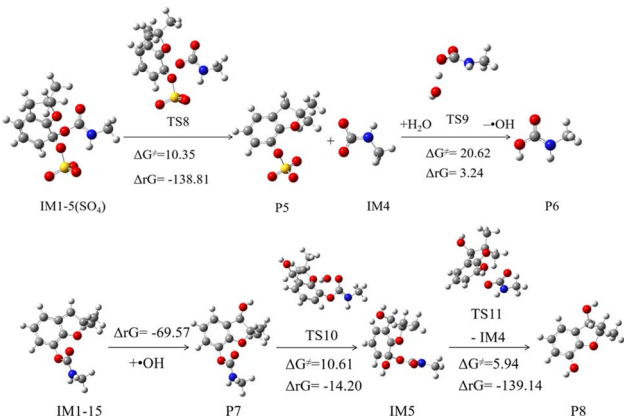

Fig. 8 Subsequent reactions of IM1-5(SO_4) and IM1-15.

generated, which corresponds to the product with m/z of 181 detected by liquid chromatography-tandem mass spectroscopy (LC-MS/MS) in the experiment.[23,55]

3.6 Ecotoxicity assessment

Studies have shown that during the degradation of pesticides using persulfate based AOPs, a large amount of more toxic parent pesticide by-products are generated.[56] Therefore, it crucial to estimate the toxicity of intermediates during pesticide degradation. ECOSAR is widely used to test the toxicity of by-products of pesticides.[57] Xu *et al.* used ECOSAR software to predict the toxicity of chlorpyrifos products after treatment with persulfate-based AOPs.[20] The results indicated that the acute and chronic toxicity of eight major degradation products to fish, aquatic invertebrates, and green algae were lower than that of the parent. Kan *et al.* predicted the acute and chronic toxicity of imidacloprid degradation products using ECOSAR software. The study found that products P1, P2, and P8 were more hazardous than the parent chemical.[58] The ECOSAR ecological toxicity model was used to predict the acute and chronic toxicity of CBF and its products to fish, water fleas, and green algae.

Table S1† lists the acute and chronic toxicity values of CBF and its degradation products. From the table, it can be seen that the chronic toxicity value of CBF to fish is 0.408 mg L^{-1}, which is

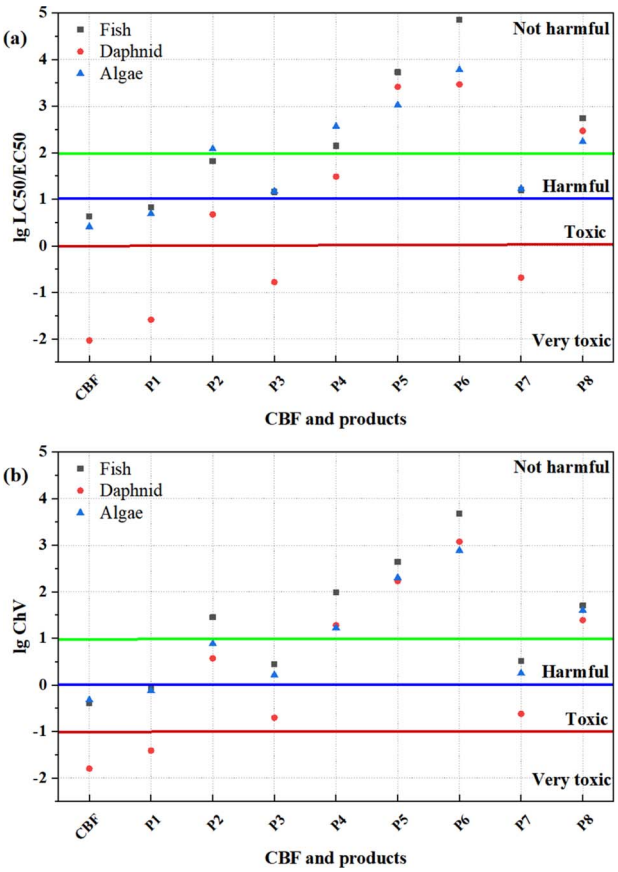

Fig. 9 Classification of acute toxicity of CBF and transformation products to aquatic organisms. (a) The acute toxicity index: LC_{50}/EC_{50} and (b) the chronic toxicity index: ChV (unit: mg L^{-1}).

consistent with the results of 0.44 mg L^{-1} for tilapia obtained by Américo-Pinheiro *et al.*[59] Fig. 9 categorizes the toxicity of CBF and its degradation products. As shown in Fig. 9(a), CBF, P1, P3, and P7 are highly toxic compounds in terms of acute toxicity to water fleas. For fish and green algae, only CBF and P1 are toxic compounds, while most of the other degradation products are harmless. In Fig. 9(b), from the perspective of chronic toxicity, only CBF and P1 are highly toxic to water fleas, while P3 and P7 are toxic compounds. For fish and green algae, most degradation products are harmless. The changes in acute and chronic toxicity indicate that the degradation products have lower acute and chronic toxicity to fish, water fleas, and green algae compared to the parent compound CBF. The main product P8 is harmless to all organisms. This result is consistent with the toxicity assessment of degradation products of CBF using persulfate-based AOPs by Samy *et al.*[23] Additionally, Singh *et al.* evaluated the ecological toxicity of CBF wastewater treated with OH radicals using algal cell vitality assays and found that the toxicity gradually decreased, with minimum toxicities of 3.04%, 4.43%, and 7.30% at 24, 48, and 72 hours, respectively.[41] This suggests that persulfate-based AOP is an effective method for remediating CBF pollution in water bodies.

4 Conclusions

This study investigated the mechanism of CBF degradation based on persulfate oxidation using DFT theory calculation methods. The optimal pathways initiated by $SO_4\cdot^-$ and ·OH were identified for degradation. Further evaluation of the toxicity of CBF degradation products was conducted to assess the feasibility of using persulfate-based AOP to degrade CBF. The results indicated that $SO_4\cdot^-$ and ·OH can undergo addition and abstraction reactions with CBF. Thermodynamic and kinetic calculations have confirmed that $SO_4\cdot^-$ and ·OH readily adds to the benzene ring, while the abstraction reaction primarily occurs on the furan ring. The initiating effect of $SO_4\cdot^-$ is greater than that of ·OH, which is consistent with experimental results. And the abstraction reaction between $SO_4\cdot^-$ and the secondary H atom on the furan ring is the optimal reaction pathway. The acute and chronic toxicity changes indicate that the degradation products exhibit lower toxicity compared to the CBF. In the products, P1, P3 and P7 still exhibits toxic or highly toxic levels, potentially posing a risk to human health. However, the primary product P8 is harmless to all organisms. The significant reduction in acute toxicity confirms that this system is a promising technology for treating CBF-contaminated water.

Data availability

The datasets supporting this article have been provided below. All the data presented in this article is present in the form of figures and tables in the manuscript itself.

Author contributions

Chenxi Zhang: conceptualization; software; data curation; writing-original draft. Youxin Xu: visualization; investigation, supervision. Bingbing Chu: software, investigation. Xiaomin Sun: methodology, supervision, writing – review & editing.

Conflicts of interest

There are no conflicts to declare.

Acknowledgements

This research was funded by the Science and Technology Development Program of Weifang City (grant number 2022GX036, 2023GX054), the Science and Technology Development Program of Shouguang City (grant number 2022JH08) and the Fundamental Research Funds of Weifang University of Science and Technology (grant number KJRC2022013).

Notes and references

1 J. Lan, W. Sun, L. Chen, H. Zhou, Y. Fan, X. Diao, B. Wang and H. Zhao, *Food Agric. Immunol.*, 2020, **31**, 165–175.
2 J. Gupta, R. Rathour, R. Singh and I. S. Thakur, *Bioresour. Technol.*, 2019, **282**, 417–424.
3 D. W. Gammon, Z. Liu and J. M. Becker, *Pest Manage. Sci.*, 2012, **68**, 362–370.
4 A. Abad, M. J. Moreno and A. Montoya, *J. Agric. Food Chem.*, 1999, **47**, 2475–2485.
5 P. O. Otieno, J. O. Lalah, M. Virani, I. O. Jondiko and K. W. Schramm, *J. Environ. Sci. Health, Part B*, 2010, **45**, 137–144.
6 S. Campbell, M. D. David, L. A. Woodward and Q. X. Li, *Chemosphere*, 2004, **54**, 1155–1161.
7 M. Umar Mustapha, N. Halimoon, W. L. Wan Johari and M. Y. Abd Shukor, *Molecules*, 2020, **25**, 2771.
8 T. P. O. Nguyen, D. E. Helbling, K. Bers, T. T. Fida, R. Wattiez, H. P. E. Kohler, D. Springael and R. De Mot, *Appl. Microbiol. Biotechnol.*, 2014, **98**, 8235–8252.
9 A. Hmimou, A. Maslouhi, K. Tamoh and L. Candela, *C. R. Geosci.*, 2014, **346**, 255–261.
10 J. H. P. Américo-Pinheiro, A. A. Machado, C. da Cruz, M. M. Aguiar, L. F. R. Ferreira, N. H. Torres and J. G. Machado-Neto, *Water, Air, Soil Pollut.*, 2020, **231**, 228.
11 S. Mishra, W. Zhang, Z. Lin, S. Pang, Y. Huang, P. Bhatt and S. Chen, *Chemosphere*, 2020, **259**, 127419.
12 N. Cao, X. Zong, X. Guo, X. Chen, D. Nie, L. Huang, L. Li, Y. Ma, C. Wang and S. Pang, *Chemosphere*, 2024, **350**, 140992.
13 K. Stoyanova, M. Gerginova, N. Peneva, I. Dincheva and Z. Alexieva, *Processes*, 2023, **11**, 3343.
14 H. Park, S. I. Seo, J.-H. Lim, J. Song, J.-H. Seo and P. I. Kim, *Metabolites*, 2022, **12**, 219.
15 R. Patowary, P. Jain, C. Malakar and A. Devi, *Environ. Sci. Pollut. Res.*, 2023, **30**, 115185–115198.
16 S. H. Alrefaee, A. M. Al-bonayan, H. H. Alsharief, M. Aljohani, K. F. Alshammari, F. A. Saad, H. M. Abumelha and N. M. El-Metwaly, *Surf. Interfaces*, 2023, **40**, 103133.

17 H. P. Toledo-Jaldin, V. Sánchez-Mendieta, A. Blanco-Flores, G. López-Téllez, A. R. Vilchis-Nestor and O. Martín-Hernández, *Environ. Sci. Pollut. Res.*, 2020, **27**, 7872–7885.
18 Z. N. Garba, A. Tanimu and Z. U. Zango, *Bull. Chem. Soc. Ethiop.*, 2019, **33**, 425–436.
19 J. M. Schöntag, A. A. Alves, L. G. Romero Esquivel and M. L. Sens, *Environ. Technol.*, 2019, **40**, 2833–2839.
20 Y. Xu, C. Zhang, H. Zou, G. Chen, X. Sun, S. Wang and H. Tian, *Toxics*, 2024, **12**, 207.
21 K. Ruíz-Hidalgo, M. Masís-Mora, E. Barbieri, E. Carazo-Rojas and C. E. Rodríguez-Rodríguez, *Chemosphere*, 2016, **144**, 864–871.
22 S. Li, Z. Liu, Z. Qu, C. Piao, J. Liu, D. Xu, X. Li, J. Wang and Y. Song, *J. Photochem. Photobiol., A*, 2020, **389**, 112246.
23 M. Samy, A. G. Kumi, E. Salama, M. ElKady, K. Mensah and H. Shokry, *Process Saf. Environ. Prot.*, 2023, **169**, 337–351.
24 Y. Aimer, O. Benali and K. G. Serrano, *Sep. Purif. Technol.*, 2019, **208**, 27–33.
25 D. Miao, S. Zhao, K. Zhu, P. Zhang, T. Wang, H. Jia and H. Sun, *Chemosphere*, 2020, **253**, 126679.
26 Z. Shen, H. Zhou, P. Zhou, H. Zhang, Z. Xiong, Y. Yu, G. Yao and B. Lai, *J. Hazard. Mater.*, 2022, **425**, 127781.
27 Y. J. Zou, X. Huang, X. L. Guo, C. H. Jia, B. T. Li, E. C. Zhao and J. X. Wu, *Ecotoxicol. Environ. Saf.*, 2022, **241**, 113815.
28 Z. Liu, X. Ren, X. Duan, A. K. Sarmah and X. Zhao, *Sci. Total Environ.*, 2023, **863**, 160818.
29 A. Romero, A. Santos, F. Vicente and C. González, *Chem. Eng. J.*, 2010, **162**, 257–265.
30 J. L. Wang and S. Z. Wang, *Chem. Eng. J.*, 2018, **334**, 1502–1517.
31 J. L. Wang and S. Z. Wang, *Chem. Eng. J.*, 2020, **401**, 126158.
32 C. Zhu, F. Liu, C. Ling, H. Jiang, H. Wu and A. Li, *Appl. Catal., B*, 2019, **242**, 238–248.
33 Z. H. Xie, C. S. He, D. N. Pei, Y. Dong, S. R. Yang, Z. Xiong, P. Zhou, Z. C. Pan, G. Yao and B. Lai, *Chem. Eng. J.*, 2023, **468**, 143778.
34 L. Wang, X. Lan, W. Peng and Z. Wang, *J. Hazard. Mater.*, 2021, **408**, 124436.
35 X. Y. Jiang, E. Kwon, H. C. Chang, N. N. Huy, X. Duan, S. Ghotekar, Y. C. Tsai, A. Ebrahimi, F. Ghanbari and K. Y. A. Lin, *Sep. Purif. Technol.*, 2023, **308**, 122789.
36 C. Zhang, Y. Xu, W. Liu, H. Zhou, N. Zhang, Z. Fang, J. Gao, X. Sun, D. Feng and X. Sun, *Ecotoxicol. Environ. Saf.*, 2023, **263**, 115298.
37 J. Yang, Y. Xu, G. Lv, T. Li and X. Sun, *J. Cleaner Prod.*, 2024, **434**, 140078.
38 A. Atifi, M. Talipov, H. Mountacer, M. D. Ryan and M. Sarakha, *J. Photochem. Photobiol., A*, 2012, **235**, 1–6.
39 I. Cwielag-Piasecka, M. Witwicki, M. Jerzykiewicz and J. Jezierska, *Environ. Sci. Technol.*, 2017, **51**, 14124–14134.
40 M. Lapertot, S. Ebrahimi, I. Oller, M. I. Maldonado, W. Gernjak, S. Malato and C. ulgarín, *Ecotoxicol. Environ. Saf.*, 2008, **69**, 546–555.
41 R. K. Singh, L. Philip and S. Ramanujam, *Ind. Eng. Chem. Res.*, 2016, **55**, 7201–7209.
42 M. J. Frisch, G. W. Trucks, H. B. Schlegel and G. E. Scuseria, *et al.*, *Gaussian 16 Rev. A.03*, Gaussian: Wallingford, CT, USA, 2016.
43 Y. Zhao and D. G. Truhlar, *Theor. Chem. Acc.*, 2008, **120**, 215–241.
44 J. Zheng, Y. Zhao and D. G. Truhlar, *J. Chem. Theory Comput.*, 2009, **5**, 808–821.
45 A. V. Marenich, C. J. Cramer and D. G. Truhlar, *J. Phys. Chem. B*, 2009, **113**, 6378–6396.
46 S. Canneaux, F. Bohr and E. Henon, *J. Comput. Chem.*, 2014, **35**, 82–93.
47 K. J. Laidler, *Theories of chemical reaction rates*, McGraw-Hill Book Company, New York, NY, USA, 1969.
48 U. S. EPA. *Ecological Structure—Activity Relationships Program (ECOSAR) Operation Manual*, vol. 2.2; U. S. EPA: Washington, DC, USA, 2022.
49 X. Y. Ding, X. Song, X. Chen, D. Ding, C. Xu and H. Chen, *Chemosphere*, 2022, **286**, 131720.
50 C. Zhang, W. Yang, J. Bai, Y. Zhao, C. Gong, X. Sun, Q. Zhang and W. Wang, *Atmos. Environ.*, 2012, **60**, 460–466.
51 B. Zhang, T. Hiramatsu, S. Hamano, M. Fujii, M. G. Alalm, S. Yoshikawa, H. Matsumoto and S. Ookawara, *J. Environ. Chem. Eng.*, 2022, **10**, 108801.
52 M. Canle Lopez, S. Rodrígez, L. F. R. Vazques, J. A. Santaballa and S. Steenken, *J. Mol. Struct.*, 2001, **565–566**, 133–139.
53 M. Canle Lopez, M. I. Fernández, S. Rodrígez, J. A. Santaballa, S. Steenken and E. Vulliet, *Phys. Chem. Chem. Phys.*, 2005, **6**, 2064–2074.
54 A. Abdelhaleem and W. Chu, *Chemosphere*, 2019, **237**, 124487.
55 K. Fouad, M. G. Alalm, M. Bassyouni and M. Y. Saleh, *Environ. Technol. Innovation*, 2021, **23**, 101778.
56 S. Khan, M. Sohail, C. Han, J. A. Khan, H. M. Khan and D. D. Dionysiou, *J. Hazard. Mater.*, 2021, **402**, 123558.
57 A. Derbalah and H. Sakugawa, *Int. J. Environ. Res.*, 2024, **18**, 11.
58 Q. Kan, K. Lu, S. Dong, D. Shen, Q. Huang, Y. Tong, W. Wu, S. Gao and L. Mao, *Environ. Pollut.*, 2020, **267**, 115438.
59 J. H. P. Américo-Pinheiro, A. A. Machado, C. da Cruz, M. M. Aguiar, L. F. R. Ferreira, N. H. Torres and J. G. Machado-Neto, *Water, Air, Soil Pollut.*, 2020, **231**, 228.